NUCL SCI TECH (2019) 30:76
https://doi.org/10.1007/s41365-019-0601-7

Development of a scintillation detector for real-time measurement of space proton effective dose

Shou-Jie Zhang[1,2] · Xin-Biao Jiang[1,2] · Da Li[1,2] · Xiao-Ren Yu[1,2] · Liang-Liang Miao[1,2] · Xiao-Jing Song[1,2,3] · Yan Ma[1,2]

Received: 23 July 2018 / Revised: 28 December 2018 / Accepted: 3 January 2019 / Published online: 10 April 2019

Abstract In this study, a scintillation detector was developed to measure the space proton effective dose for astronauts based on the proton effective dose conversion coefficients provided by International Commission on Radiological Protection Report No. 116. In the Monte Carlo N-Particle Transport Code X (version 2.6.0) simulation process, by modulating the depth and solid angle of truncated conical holes in an iron shell from lower-energy protons to higher-energy protons, the energy deposited in the scintillator by isotropic protons was nearly proportional to the corresponding effective dose, with a maximum relative deviation of 13.28% at thirteen energy points in the energy range of 10–400 MeV. Therefore, the detector can monitor proton effective dose indirectly in real time by measuring the deposited energy. We calibrated the photoelectric conversion efficiency of the detector at the cobalt source, tested the response of the detector in the energy range of 30–100 MeV in unidirectional proton field, and validated the simulation with the experimental results.

This work was supported by the National Natural Science Foundation of China (No. 11305127), and the State Key Lab of Intense Pulsed Radiation Simulation and Effect Basic Research Foundation (No. SKLIPR1216).

✉ Shou-Jie Zhang
15996252960@163.com

1 Northwest Institute of Nuclear Technology, Xi'an 710024, China

2 State Key Laboratory of Intense Pulsed Radiation Simulation and Effect, Xi'an 710024, China

3 Xi'an Jiaotong University, Xi'an 710049, China

Keywords Effective dose · Space proton · Scintillation detector · ICRP Report No. 116 · Deposited energy

1 Introduction

Radiation exposure is one of the most significant health concerns to astronauts [1, 2]. During their occupational activities in space, astronauts suffer ionizing radiation, which is likely to induce stochastic effects such as cancers and hereditary effects [3–5]. Effective dose can assess the risk of stochastic effects caused by ionizing radiation, so it is often adopted as a dose limit for astronauts [6]. Presently, the dosimeters used in space dosimetry are primarily classified into two categories: passive dosimeters such as thermoluminescence dosimeters (TLD), plastic nuclear track detectors (PNTD), and nuclear emulsion detectors; and active dosimeters such as tissue equivalent proportional counters (TEPC), silicon semiconductor detectors, and dosimetry telescopes (DOSTEL). These two categories of dosimeters are both focused on dose quantity of absorbed dose and dose equivalent rather than effective dose [7–11]. In some low Earth orbit missions, the experimental procedure of effective dose measurement was performed by life-size human phantoms, which usually contained combined dosimeter packages consisting of dozens of passive dosimeters to measure organ dose equivalents [12–14]. The entire detection system of this method is too heavy and bulky for space applications. Furthermore, passive dosimeters cannot reflect the accurate change in dose rate over time; therefore, this method cannot achieve real-time measurement of effective dose in space.

Protons are the main component of space charged particles as well as a significant contributor to radiation hazards for astronauts [15]. Space proton radiation models have various limitations and are not accurate enough for space proton effective dose assessment, which has appreciable significance for the radiation safety of astronauts. For example, the deviation of proton fluence at low-altitude orbit is as much as 10 times that of the Aerospace Proton Environmental Model 9 (AP9 model) compiled by National Aeronautics and Space Administration (NASA). The model is based on average and static methods that do not reflect structure details and variation in the radiation environment. Moreover, the monitoring area of the model cannot cover the entire near-Earth space [16, 17]. In light of the above-mentioned facts, it is desirable to develop a detector for proton effective dose measurement.

The 2010 International Commission on Radiological Protection (ICRP) Report No. 116 (ICRP-116) provided the conversion coefficients between proton fluence and proton effective dose for standard irradiation geometries [18]. These coefficients were calculated using the official ICRP and International Commission on Radiation Units and Measurements (ICRU) computational phantoms representing the reference adult male and reference adult female [19, 20], in conjunction with Monte Carlo codes simulating the transport of radiation within the human body. Simulations were performed by members of several task groups using different Monte Carlo codes. In this study, we aimed to design a detector with rather small volume and mass for real-time measurement of space proton effective dose based on the ICRP-116. The design principle and process of the detector are described in detail, as well as the detector calibration and verification experiment.

2 Modeling and analysis

2.1 Detector probe design principle

Effective dose, E, is defined as follows:

$$E = \sum_{\mathrm{T}} w_{\mathrm{T}} H_{\mathrm{T}} = \sum_{\mathrm{T}} w_{\mathrm{T}} \sum_{\mathrm{R}} w_{\mathrm{R}} D_{\mathrm{T,R}} = \sum_{\mathrm{T}} w_{\mathrm{T}} \sum_{\mathrm{R}} w_{\mathrm{R}} \left(\frac{1}{m_{\mathrm{T}}} \int_{m_{\mathrm{T}}} D_{\mathrm{R}} \mathrm{d}m \right), \tag{1}$$

where w_{T} and w_{R} are the tissue weighting factor and radiation weighting factor, respectively, H_{T} is the equivalent dose in an organ or tissue T, $D_{\mathrm{T,R}}$ is the mean absorbed dose in an organ or tissue T from radiation of type R, m_{T} is the mass of the organ or tissue T and D_{R} is the absorbed dose in a mass element dm. It is difficult to measure $D_{\mathrm{T,R}}$ directly, and for this reason, the effective dose is hard to monitor.

The conversion coefficients between proton fluence and proton effective dose for standard irradiation geometries provided by the ICRP-116 are presented in Fig. 1 [18].

For a certain amount of incident protons whose energy is X, the corresponding effective dose $E(X)$ can be obtained according to the ICRP-116, the energy deposited in the detector by these protons is $Q(X)$, if the coefficient $K(X)$ between $E(X)$ and $Q(X)$ does not change with energy X, in other words, $Q(X)$ is proportional to $E(X)$, that is,

$$K(X) = E(X)/Q(X) = K = \mathrm{Const.} \tag{2}$$

Then in practice, multiplying the measured deposited energy Q by the coefficient K, we can get the actual effective dose E for astronauts:

$$E = K \times Q. \tag{3}$$

Presently, the orbit height of manned spaceflight is mainly in the range of 300–500 km, which is referred to as low Earth orbit, or LEO. The energy of protons of LEO is mostly below 400 MeV [21, 22]. Based on the thirteen conversion coefficients between proton fluence and proton effective dose provided by the ICRP-116 in the energy range of 10–400 MeV, our aim is to make the energy deposited in the detector proportional to the corresponding effective dose of the incident protons.

2.2 Detector probe design process

2.2.1 Basic structure and materials

Since 1955, five solar particle events (SPEs) with intensities and energies large enough to jeopardize crew health in spite of normal or even enhanced spacecraft shielding have been observed. The order of magnitude of

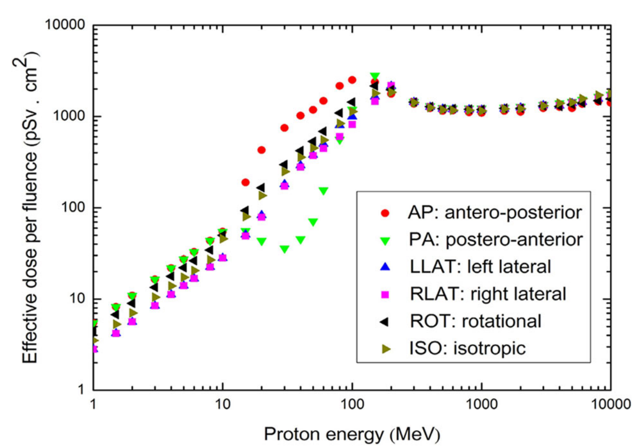

Fig. 1 (Color online) Effective dose per proton fluence for standard geometries

the integral of the fluence of protons above 10 MeV in these SPEs is 10^{10} cm^{-2} [23]. This is only an order of magnitude smaller than the proton dose threshold (2.0×10^{11} cm^{-2}) inducing radiation damage in semiconductor detectors. This amount of radiation damage can cause an increase in leakage current, degradation of energy resolution, and a shift in the peak position because of lost charge collection efficiency [24]. Consequently, the performance of semiconductor detectors will gradually degrade and eventually lose function after lengthy exposure in space. The proton-stopping power of gas is rather small owing to its low density [25], so the volume and pressure of a gas detector would be rather large for the detection of high-energy protons, and this leads to the poor security and practicability of a gas detector in the space environment. The absorbed dose in space measured by the phantom torso experiment in the 9.8-day STS-91 mission (inclination: 51.6°, altitude: 400 km) was 27.7 mGy, or 2.8 mGy/d [12]. Experimental results showed that, at a proton absorbed dose of 1 KGy, the radiation damage reduced the light yield of a plastic scintillator by only 15% [26], which reflected the plastic scintillator's characteristics of stable luminescence efficiency and good radiation hardness. Plastic scintillator material also has the characteristics of good plasticity and high mechanical strength, which enable it to be processed into various shapes [27].

Isotropic exposure is the most realistic situation in space. While shielding effects may result in lower isotropic exposure, the movement of the astronauts within the spacecraft counteracts this [15], so the proton incidence condition was set as isotropic in the simulation. Based on this, a spherically symmetric detector was desired, so the scintillator was set as a sphere whose radius was 2.25 cm. A cylindrical light guide was used with the scintillator to aid the light collection for the detector. The radius and length of the light guide were 1.0 cm and 10.3 cm, respectively, and the distance from the center of the scintillator to the lower end surface of the light guide was 2.0 cm. Covering the spherical scintillator was a layer of shielding shell, inside which were some truncated conical holes. The energy deposited in the scintillator was modulated by changing the depth and solid angle of these holes. The greater the number of holes, and the more spherical the distribution of the holes in the shielding shell, the better was the spherical symmetry of the detector. Considering the similarity between the geometry of a regular polyhedron and a sphere, the holes in the shielding shell were effectively located at the vertices of a regular polyhedron. In the existing five types of regular polyhedrons, the regular dodecahedron has the greatest number of vertices (20). The two adjacent holes near the light guide were integrated into one to minimize their conflict with the light guide in space, leaving 19 holes in the iron shell. Except for the integrated hole around the light guide (hole 1), the other 18 holes were located at 18 vertices of a regular dodecahedron. The structure of the detector probe and sequence numbers of some of the holes are shown in Fig. 2a. The relative distribution of the 19 holes and their corresponding sequence numbers in the regular dodecahedron are shown in Fig. 2b, where three different colors indicate three different depth holes.

Figure 3 shows the range–energy relation and the mass thickness–energy relation of protons in different materials; the data are from NIST's PSTAR databank (CSDA) [28]. From Fig. 3, we can see that for protons with a certain energy, the range in Fe is almost the same as that in Cu and Pb, and far less than that in Be and Al. However, the mass thickness in Fe is less than that in Cu and Pb. To reduce the mass and volume of the detector, iron was adopted as the material of the shielding shell.

2.2.2 Determination of the iron shell thickness

Before digging holes in the iron shell, we needed to determine the iron shell thickness. Figure 4 presents the MCNPX simulation results of the dependence of $Q_{400\mathrm{MeV}}$ on the shell thickness, as the thickness varies from 0 to 3 cm, where $Q_{400\mathrm{MeV}}$ is the energy deposited in the scintillator by per fluence of isotropic incident protons of 400 MeV.

As shown in Fig. 4, the value of $Q_{400\mathrm{MeV}}$ at $d = 0$ cm is 86% of that at $d = 3$ cm. $Q_{400\mathrm{MeV}}$ remains nearly constant because protons of 400 MeV have strong penetrating power and the energy loss rate in the plastic scintillator is almost the same after it passes through the iron shell of different thicknesses. Consequently, the coefficient K between effective dose and deposited energy is determined:

$$K = K_{400\mathrm{MeV}} = E_{400\mathrm{MeV}}/Q_{400\mathrm{MeV}}. \tag{4}$$

By modulating the depth and solid angle of the 19 shell holes, we attempted to make the deposited energy Q at the other 12 twelve energy points, apart from 400 MeV, satisfy the proportional relation with the corresponding effective dose E. Relative deviation ε between Q and E is defined in Formula (5) to assess the proportional relation. The smaller the value of $|\varepsilon|$, the better is the proportional relation.

$$\varepsilon = K \cdot \frac{Q}{E} - 1 \tag{5}$$

For protons of 150 MeV, 200 MeV, and 300 MeV, Fig. 5 presents the MCNPX simulation results of the dependence of ε on the uniform iron shell thickness. It is shown that when $d < 2.5$ cm, $\varepsilon_{150\mathrm{MeV}} > 0$; thus, d must be larger than 2.5 cm. If we want to reduce $\varepsilon_{150\mathrm{MeV}}$ to zero, we can select a value of d in the range of 2.5–2.9 cm. Here we chose 2.9 cm to make $|\varepsilon_{150\mathrm{MeV}}|$ as small as possible. The

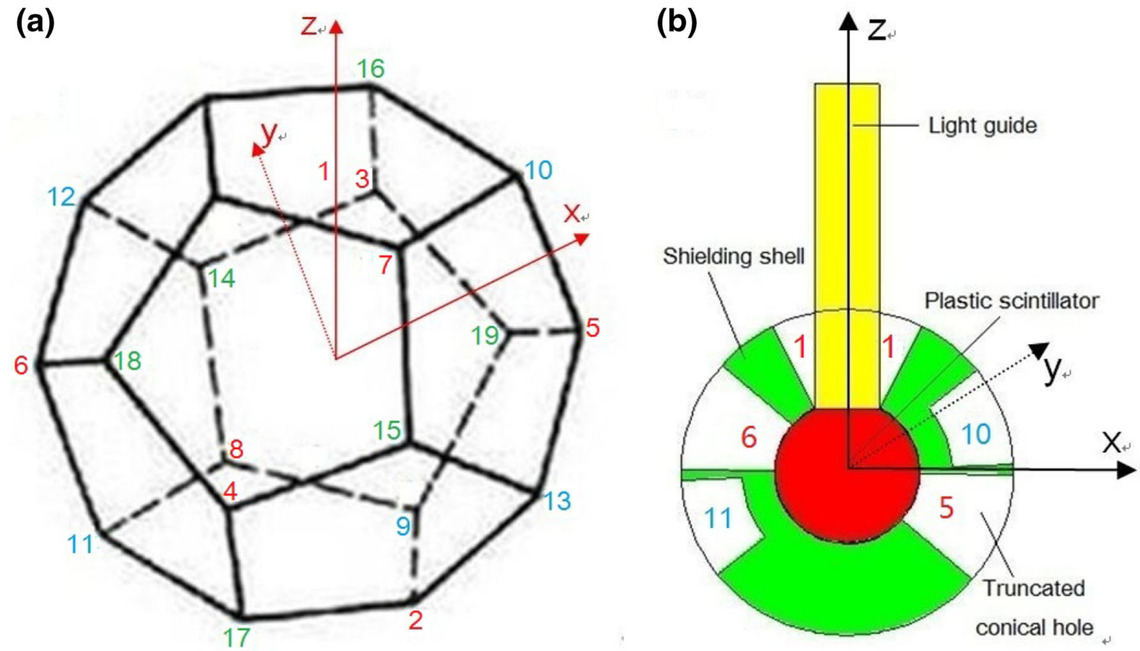

Fig. 2 (Color online) **a** Cross-sectional view of the detector probe. **b** Relative distribution of the 19 holes in the dodecahedron

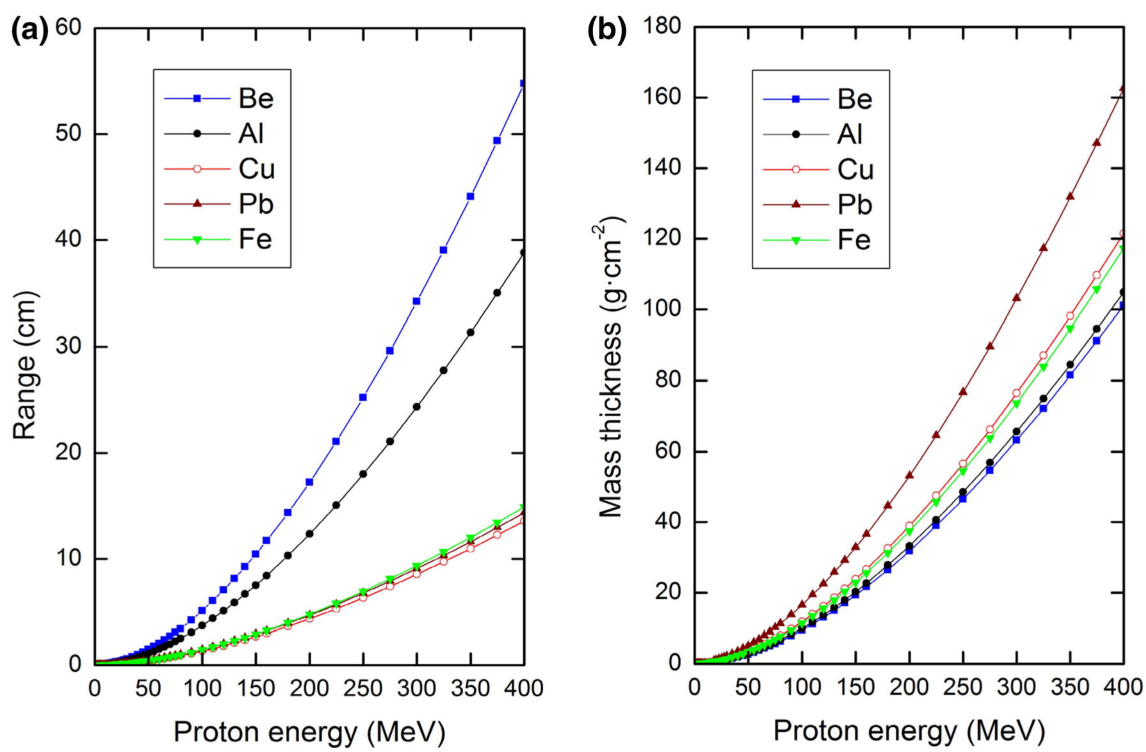

Fig. 3 (Color online) Penetration depth of proton in different materials. **a** Range; **b** mass thickness

method we adopted was to adjust the depth and solid angle of the holes to be dug in the future design, using the positive $\varepsilon_{150\mathrm{MeV}}$ of the perforated zone (where the covering thickness is less than 2.5 cm) to compensate for the negative $\varepsilon_{150\mathrm{MeV}}$ (− 88%) of the non-perforated zone (where the covering thickness is 2.9 cm). The tendency of the change in $\varepsilon_{200\mathrm{MeV}}$ with iron shell thickness opposes that of $\varepsilon_{150\mathrm{MeV}}$, $\varepsilon_{200\mathrm{MeV}} < 0$ when $d < 0.9$ cm, and $\varepsilon_{200\mathrm{MeV}} > 0$ when $d > 0.9$ cm. $\varepsilon_{300\mathrm{MeV}}$ is very small when d varies from 0 to 2.9 cm.

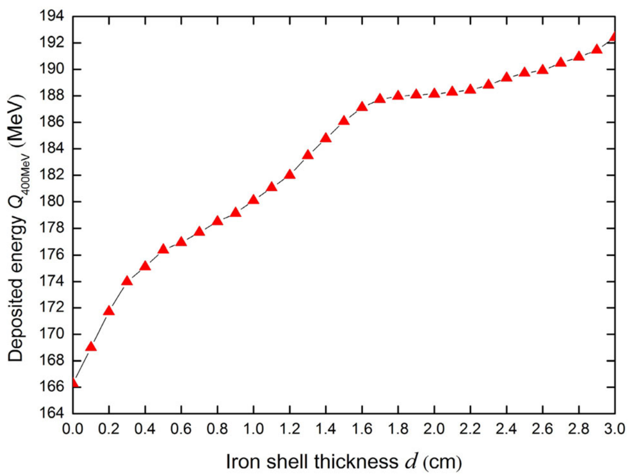

Fig. 4 Dependence of the deposited energy in the scintillator on the iron shell thickness

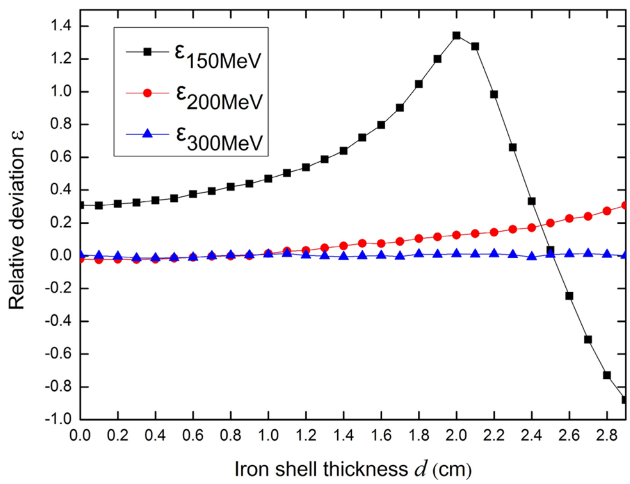

Fig. 5 Dependence of the relative deviation between deposited energy and proton effective dose on the iron shell thickness

2.2.3 Determination of depth and solid angles of the holes

First we dug the holes whose sequence numbers are from 1 to 8, with depths and covering thicknesses of 2.9 cm and 0 cm, respectively. For protons from 10 to 80 MeV, Fig. 6 shows the MCNPX simulation results of the dependence of ε on $\sum \Omega_1$, where $\sum \Omega_1$ denotes the total solid angle of these eight holes. From Fig. 6, we can see that when $\sum \Omega_1 < 3.355$ Sr, $\max(|\varepsilon_{15\mathrm{MeV}}|, |\varepsilon_{30\mathrm{MeV}}|) = -\varepsilon_{30\mathrm{MeV}} > 13\%$, and when $\sum \Omega_1 > 3.355$ Sr, $\max(|\varepsilon_{15\mathrm{MeV}}|, |\varepsilon_{30\mathrm{MeV}}|) = \varepsilon_{15\mathrm{MeV}} > 13\%$. $\max(|\varepsilon_{15\mathrm{MeV}}|, |\varepsilon_{30\mathrm{MeV}}|)$ is minimized to 13% when $\sum \Omega_1$ is 3.355 Sr, and $|\varepsilon|$ for protons of 10 MeV, 20 MeV, 40 MeV, 50 MeV, 60 MeV, and 80 MeV is within 13% when $\sum \Omega_1$ is 3.355 Sr.

Next we dug the holes whose sequence numbers are from 9 to 13, with depths and covering thicknesses of

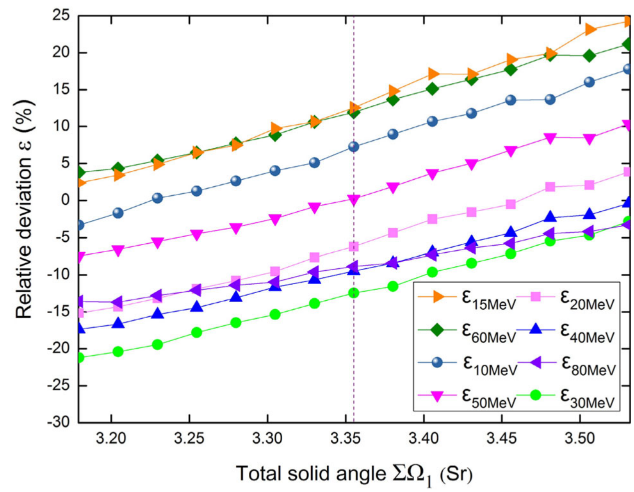

Fig. 6 (Color online) Dependence of the relative deviation between deposited energy and proton effective dose on total solid angle of holes 1–8

1.9 cm and 1.0 cm, respectively. Modulation of the solid angle of these five holes would not affect the deposited energy of the protons below 80 MeV because these protons cannot penetrate holes 9–13 because their range in iron is less than 1.0 cm. Figure 7 shows the MCNPX simulation results of the dependence of $\varepsilon_{100\mathrm{MeV}}$ on $\sum \Omega_2$, where $\sum \Omega_2$ denotes the total solid angle of these five holes. We can see that $|\varepsilon_{100\mathrm{MeV}}|$ is minimized to 0.54% when $\sum \Omega_2$ is 1.508 Sr. The MCNPX computational accuracy of the deposited energy of protons of 100 MeV is less than 1%, which is comparable to the minimum value of $|\varepsilon_{100\mathrm{MeV}}|$.

Next, we dug the holes whose sequence numbers are from 14 to 19, with depths and covering thicknesses of 1.4 cm and 1.5 cm, respectively. Modulation of the solid angle of these six holes would not affect the deposited energy of the protons below 100 MeV because these

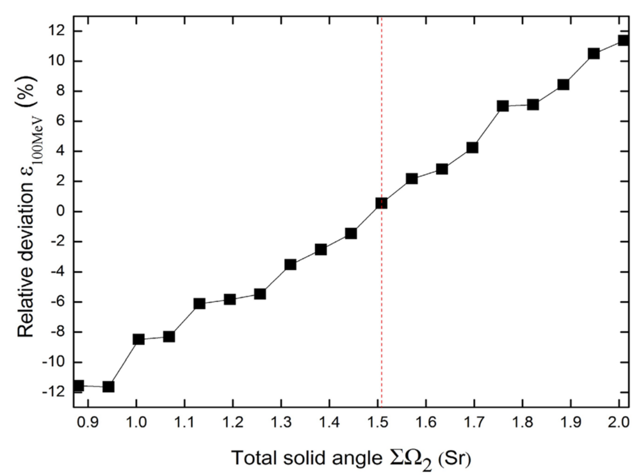

Fig. 7 Dependence of the relative deviation between deposited energy and proton effective dose on total solid angle of holes 9–13

protons cannot penetrate holes 14–19 because their range in iron is less than 1.5 cm. For protons of 150 MeV, 200 MeV and 300 MeV, Fig. 8 shows the MCNPX simulation results of the dependence of ε on $\sum\Omega_3$, where $\sum\Omega_3$ denotes the total solid angle of these six holes. Figure 8 shows that $\max(|\varepsilon_{150\mathrm{MeV}}|, |\varepsilon_{200\mathrm{MeV}}|)$ is minimized to 13% when $\sum\Omega_3$ is 2.136 Sr, and $|\varepsilon_{300\mathrm{MeV}}|$ is close to zero.

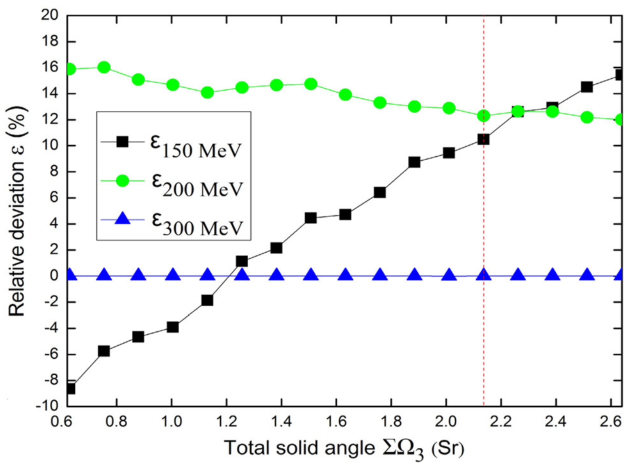

Fig. 8 Dependence of the relative deviation between deposited energy and proton effective dose on total solid angle of holes 14–19

2.3 Calculation results and analysis

Geometrical parameters of the 19 holes are shown in Table 1, where $\theta_1/\theta_2/\theta_3$ are the angles between the hole axis and the *x*/*y*/*z* axes, respectively. A prototype of the detector probe was constructed by 3D printing technology according to the design scheme described in Sect. 2.2. A stereogram of the detector probe and cross-sectional view of the iron shell are shown in Fig. 9a, b, respectively. Sequence numbers of some of the holes are marked in the figure.

$K_{400\mathrm{MeV}}$ was used as the coefficient K in the simulation process, to reduce the maximum absolute value of ε, regarded as a function of the coefficient K at the selected 13 energy points,

$$\max\{|\varepsilon|_{i=1:13}\} = f(K) = \max\left\{\left|K\frac{Q_i}{E_i} - 1\right|_{i=1:13}\right\}, \quad (6)$$

where the subscript i from 1 to 13 represents the selected energy point. The minimum of $f(K)$ and the corresponding value K_0 of K when $f(K)$ reaches the minimum can be calculated, and the calculation results are shown in Table 2, from which we can see that $\max\{|\varepsilon|_{i=1:13}\}$ is reduced from 13.93 to 13.28% after $K_{400\mathrm{MeV}}$ is replaced by K_0. Figure 10a shows the proton effective dose per fluence from the literature and calculation, and the deviation between them is presented in Fig. 10b.

Table 1 Geometrical parameters of the 19 holes (hole 1 was the integrated hole)

Sequence number of the hole	$\theta_1/\theta_2/\theta_3$ (°)	Depth (cm)	Covering thickness (cm)	Solid angle (Sr)	Total solid angle $\sum\Omega$ (Sr)
1	90.0/90.0/0.0	2.9	0.0	0.6656	3.355
2	90.0/110.9/159.1	2.9	0.0	0.3842	
3	69.1/20.9/90.0	2.9	0.0	0.3842	
4	110.9/159.1/90.0	2.9	0.0	0.3842	
5	20.9/90.0/110.9	2.9	0.0	0.3842	
6	159.1/90.0/69.1	2.9	0.0	0.3842	
7	54.7/125.3/54.7	2.9	0.0	0.3842	
8	125.3/54.7/125.3	2.9	0.0	0.3842	
9	90.0/69.1/159.1	1.9	1.0	0.3016	1.508
10	20.9/90.0/69.1	1.9	1.0	0.3016	
11	159.1/90.0/110.9	1.9	1.0	0.3016	
12	125.3/54.7/54.7	1.9	1.0	0.3016	
13	54.7/125.3/125.3	1.9	1.0	0.3016	
14	110.9/20.9/90.0	1.4	1.5	0.3560	2.136
15	69.1/159.1/90.0	1.4	1.5	0.3560	
16	54.7/54.7/54.7	1.4	1.5	0.3560	
17	125.3/125.3/125.3	1.4	1.5	0.3560	
18	125.3/125.3/54.7	1.4	1.5	0.3560	
19	54.7/54.7/125.3	1.4	1.5	0.3560	

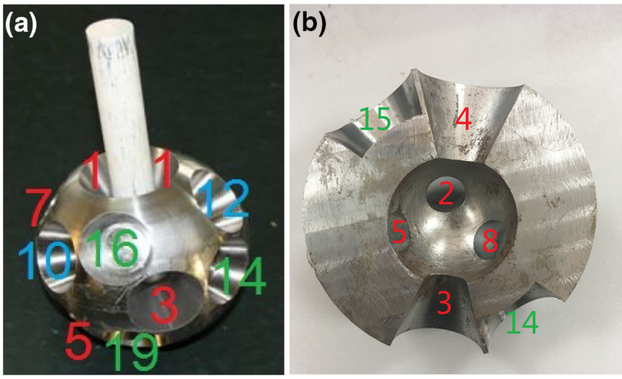

Fig. 9 (Color online) **a** picture of the detector probe; **b** cross-sectional view of the iron shell

3 Experimental study

3.1 Detection system

The detection system is composed of a detector probe, phototube, and electrometer. The scintillator is an HND-S2 plastic scintillator whose luminescence spectrum is shown in Fig. 11. Its luminous attenuation length is larger than 2 m, and its density is 1.05 g/cm^3. Its luminescence efficiency falls by only 15% when the fluence of fast neutrons reaches 1×10^{13} neutrons/cm^2 and remains nearly constant after the exposure of ^{60}Co gamma photons reaches 25.8 C/kg. The scintillator has the characteristics of high transparency, small density, and good radiation hardness. The light guide is made of polymethyl methacrylate (PMMA), which does not scintillate from impinging protons. The phototube is of type GD40H, whose window and cathode materials are borosilicate glass and bialkali (KCsSb), respectively. Its spectral response range is 300–650 nm, with a peak wavelength of 400 nm. The spectral response curve of the phototube has a large overlapping range with the luminescence spectrum curve of the scintillator; the peak wavelengths of the two curves are close to each other, and the phototube can make the best use of the light emitted from the scintillator. The electrometer is a Keithley 6517B electrometer manufactured by Keithley Corporation of America. Its charge measurement sensitivity is 10 fC, and it has the characteristics of high sensitivity and low noise. Deposited energy in the plastic scintillator is converted to electric charge, which is measured by the electrometer.

3.2 Calibration of the detector photoelectric conversion efficiency

The relation between deposited energy and response of the detector is as follows:

$$q_{\mathrm{H}} = Q_{\mathrm{H}} \cdot Y_{\mathrm{H}} \cdot F_{\mathrm{ph}} \cdot \mu \cdot e, \tag{7}$$

where q_{H} is the quantity of electric charge measured by the electrometer (C), Q_{H} is the deposited energy (MeV) and Y_{H} is the scintillator light yield for protons, or the number of photons generated per MeV (MeV^{-1}). The scintillation light output for the HND-S2 plastic scintillator we adopted is proportional to the proton energy, so Y_{H} was taken as constant in this work (8.8×10^3 MeV^{-1}, 20 °C). F_{ph} is the light transfer efficiency in the scintillator and the light guide (dimensionless). μ is the average quantum efficiency of the incident light on the cathode of the phototube

Table 2 Calculation results of the MCNPX simulation

Proton energy (MeV)	Effective dose E per fluence of isotropic protons (pSv cm^2)	Deposited energy Q by per fluence of isotropic protons (MeV cm^2)	MCNPX computational accuracy of Q (%)	$K_{400\mathrm{MeV}} \times \frac{Q}{E} - 1$ (%)	$K_0 \times \frac{Q}{E} - 1$ (%)
10	45.8	7.11533E+00	0.39	5.20	4.59
15	80.1	1.31069E+01	0.40	10.80	10.17
20	136	1.90570E+01	0.44	− 5.11	− 5.66
30	249	3.20749E+01	0.44	− 12.77	− 13.28
40	358	4.77748E+01	0.41	− 9.63	− 10.16
50	451	6.77786E+01	0.43	1.77	1.18
60	551	9.27070E+01	0.42	13.93	13.28
80	837	1.23035E+02	0.38	− 0.46	− 1.04
100	1130	1.75599E+02	0.31	5.23	4.62
150	1790	2.93486E+02	0.26	11.03	10.39
200	1840	3.05358E+02	0.24	12.38	11.73
300	1420	2.10285E+02	0.26	0.28	− 0.30
400	1250	1.84596E+02	0.28	0	− 0.58

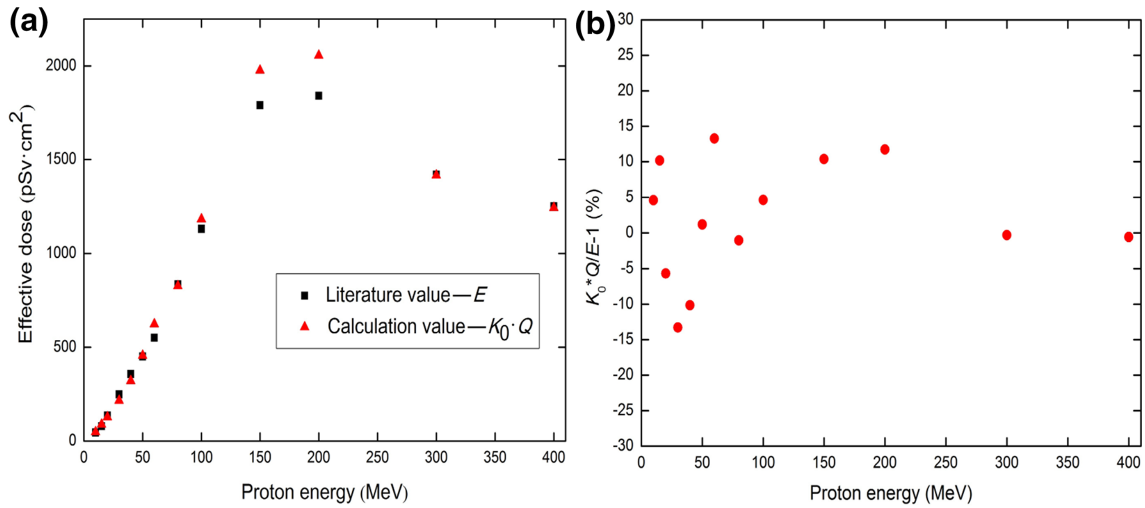

Fig. 10 **a** Proton effective dose from the literature and calculation; **b** deviation between the literature and calculation

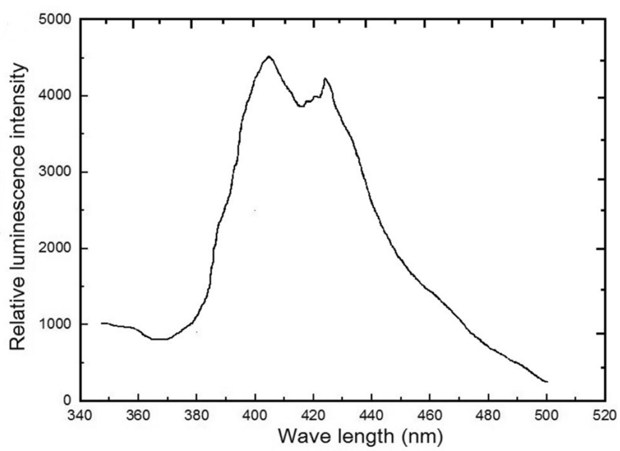

Fig. 11 Luminescence spectrum of the HND-S2 plastic scintillator

Table 3 Calibration results of the detector photoelectric conversion efficiency

d (m)	Q_γ (MeV)	q_γ (C)	Y_γ (MeV^{-1})	η (%)
0.7	6.06×10^9	49.00×10^{-9}	1.06×10^4	0.48
1.0	2.94×10^9	24.20×10^{-9}	1.06×10^4	0.49
1.5	1.34×10^9	10.80×10^{-9}	1.06×10^4	0.48
2.0	0.72×10^9	6.25×10^{-9}	1.06×10^4	0.51

(dimensionless). e is the elementary charge (C). The product of F_{ph} and μ is defined as the detector's photoelectric conversion efficiency η, which can be calibrated on a cobalt source:

$$\eta = F_{ph} \cdot \mu = \frac{q_\gamma}{Q_\gamma \cdot Y_\gamma \cdot e}, \tag{8}$$

where q_γ is the response of the detector when it is exposed to a cobalt source, and Q_γ is the deposited energy of gamma rays in the scintillator and is calculated using the MCNPX program based on the calibration experimental condition. Y_γ is the scintillator light yield for gamma rays, provided by the corporation that manufactured the scintillator. The calibration experiment was performed in a ^{60}Co γ-radiation field of Northwest Institute of Nuclear Technology (NINT). The calibration results of the detector photoelectric conversion efficiency are shown in Table 3, where d is the distance from the center of the detector probe to the cobalt source.

3.3 Verification experiment

Isotropic irradiation is an ideal condition. Taking into account the reality, the detector was irradiated in unidirectional proton field. The verification experiment was performed on the platform of the HI-13 tandem accelerator upgrading project of the China Institute of Atomic Energy. The platform can provide unidirectional proton beams in the energy range of 30–100 MeV, with irradiation area of 75 mm × 75 mm [29]. The detector was irradiated on the platform from four directions: antero-posterior (AP, x), postero-anterior (PA, $-x$), left lateral (LLAT, $-y$), and right lateral (RLAT, y). The irradiation directions with respect to the detector probe are defined in Fig. 12. The four irradiation directions (PA/AP/LLAT/RLAT) were set normal to the common axis of the light guide and phototube to prevent direct irradiation of the phototube by the proton beam.

Deposited energy Q_H in the scintillator in the experimental proton field can be calculated by the MCNPX program [30]. The shielding effect of the light guide and

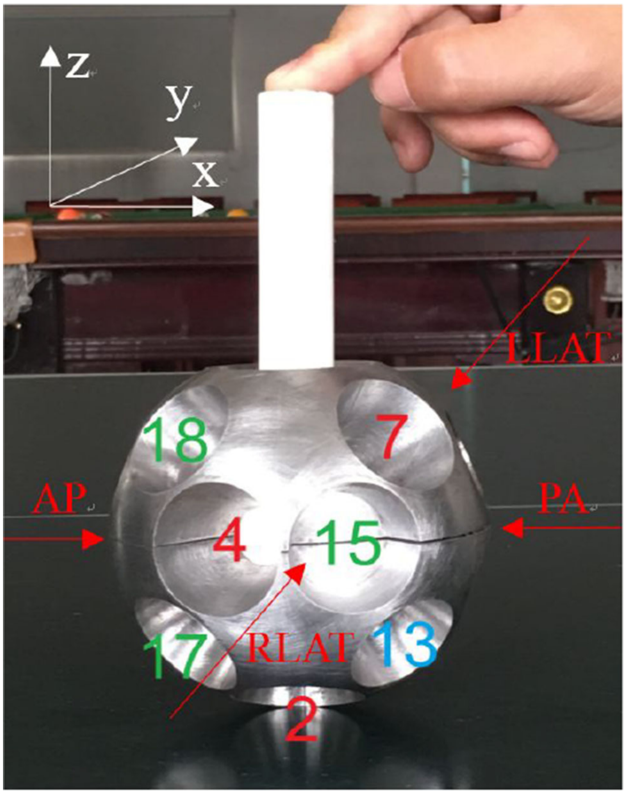

Fig. 12 (Color online) Different irradiation directions with respect to the detector probe

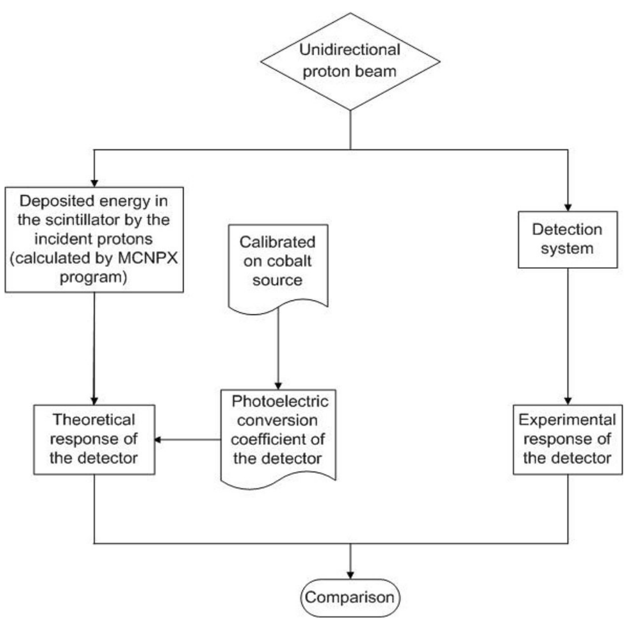

Fig. 13 Total frame diagram of the verification experiment

both energy straggling and angle straggling effects of the proton beams had already been considered in the calculation model. Combined with the calibrated detector photoelectric conversion efficiency, the theoretical response q_{H} of the detector can be obtained by Eq. (7). The theoretical response q_{H} and the experimental response q'_{H} were compared to verify the detector design, as shown in Fig. 13.

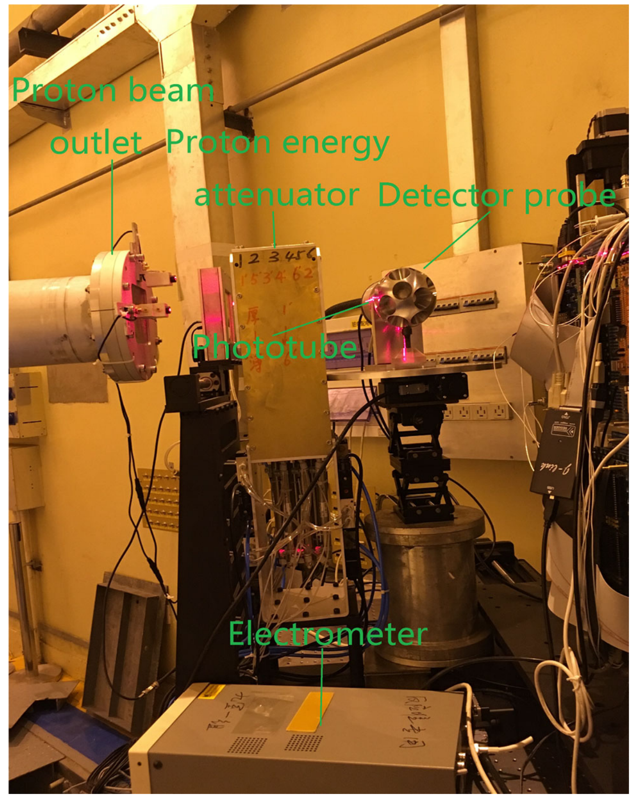

Fig. 14 (Color online) Detector design verification experimental site

Figure 14 shows the experimental setup. The deviation δ between the theoretical response and the experimental response of the detector is presented in Table 4, where $\delta = \left(q_{\mathrm{H}} - q'_{\mathrm{H}}\right)/q'_{H}$.

The difference between calculation and measurement ranges from $-$ 18.70 to 17.53% as shown in Table 4. Considering the stability of the proton beam intensity, temperature effects of the scintillator light yield, and proton radiation damage to the scintillator during the experiment, Formula (7) can be transformed into

$$q_{\mathrm{H}} = \int_{0}^{t_0} I_{\mathrm{H}}(t) \cdot \overline{Q_{\mathrm{H}}} \cdot Y_{\mathrm{H}}(T(t), D(t)) \cdot \eta \cdot e\mathrm{d}t, \tag{9}$$

where t_0 (s) is the duration of each irradiation in Table 4, $I_{\mathrm{H}}(t)$ (protons/s) is the proton beam intensity at time t, $\overline{Q_{\mathrm{H}}}$ (MeV) is the deposited energy in the scintillator of each source proton calculated using the MCNPX program, $T(t)$ (K) is the temperature of the scintillator at time t, and $D(t)$ (Gy) is the accumulated absorbed dose of the scintillator at time t.

If we neglect scintillator heat dissipation in each irradiation process and assume that all of the deposited energy was

Table 4 Detector design verification experimental results

Proton energy (MeV)	AP			PA			LLAT			RLAT		
	q_H ($\times 10^{-9}$ C)	q'_H ($\times 10^{-9}$ C)	δ (%)	q_H ($\times 10^{-9}$ C)	q'_H ($\times 10^{-9}$ C)	δ (%)	q_H ($\times 10^{-9}$ C)	q'_H ($\times 10^{-9}$ C)	δ (%)	q_H ($\times 10^{-9}$ C)	q'_H ($\times 10^{-9}$ C)	δ (%)
30	16.5	17.6	− 6.25	25.9	25.3	2.37	15.2	13.9	9.35	18.1	15.4	17.53
40	26.2	28.0	− 6.43	40.6	44.8	− 9.38	24.2	24.3	− 0.41	28.4	25.7	10.51
50	872.3	860.2	1.41	1401.0	1632.4	− 14.18	804.5	733.2	9.72	1010.5	1044.5	− 3.26
60	1246.6	1120.3	11.27	2017.5	2241.8	− 10.01	1143.8	1092.3	4.71	1414.7	1386.1	2.06
70	1723.3	1854.0	− 7.05	2757.4	2984.5	− 7.61	1562.6	1425.3	9.63	1914.2	1872.5	2.23
80	1728.4	1857.4	− 6.95	2806.5	3349.7	− 16.22	1574.2	1585.4	− 0.71	1922.5	2143.8	− 10.32
90	2088.3	2142.7	− 2.54	3379.0	3249.7	3.98	1610.5	1515.6	6.26	1982.3	2242.4	− 11.60
100	2783.8	2585.0	7.69	4457.6	3865.0	15.33	1709.1	1750.6	− 2.37	2066.1	2541.2	− 18.70

converted into heat, which raised the temperature of the scintillator, then the maximum temperature rise of the scintillator would be $\Delta T = I_{\mathrm{H}} \cdot t_0 \cdot \overline{Q_{\mathrm{H}}}/(m \cdot c) = 1.56 \times 10^{-3}$ K (PA, 100 MeV), where $c = 1330$ J kg^{-1} K^{-1} is the specific heat capacity of the scintillator, $m = 0.0497$ kg is the mass of the scintillator, $I_{\mathrm{H}} = 2.5 \times 10^9$ protons/s, $t_0 = 60$ s, and $\overline{Q_{\mathrm{H}}} = 4.30736$ MeV. Within − 50 to 100 °C, the temperature coefficient of the scintillator light yield is 0.068%/K; therefore, in the experiment, the change in the scintillator light yield caused by its own temperature rise is negligible. In the experiment, if we take the proton beam intensity as constant (2.5×10^9 protons/s) and neglect its fluctuation (within ± 15%), then the accumulated absorbed dose of the scintillator over 32 irradiations is $\sum D = \sum I_{\mathrm{H}} \cdot t_0 \cdot \overline{Q_{\mathrm{H}}}/m = 3.6$ Gy, which is so small that its influence on the light yield and optical transmittance of the scintillator is negligible [26]. The theoretical response of the detector was proportional to the proton beam intensity, whose fluctuation (within ± 15%) during the experiment was the dominant cause of the difference between the calculated and measured results.

4 Conclusion

In this study, an indirect space proton effective dose measurement method was first proposed based on the ICRP-116. The scintillation detector was simulated by the MCNPX program for 10–400 MeV protons, and the deposited energy was nearly proportional to the corresponding effective dose provided by the ICRP-116. A prototype of the detector was constructed to conduct a verification experiment on the platform of the HI-13 tandem accelerator upgrading project of the China Institute of Atomic Energy. Experimental results validated the feasibility of the theoretical design of the detector, to some extent. Future work will consider a different type of scintillator with larger density and smaller volume; hence, the reduced mass and volume will address the expensive launch of manned spaceflights. The detector probe will be shaped to a more spherical design such as a buckyball to achieve a more precise simulation of the isotropic irradiation condition of astronauts in space, and the radiation hazard to astronauts from particles other than protons in space will be estimated.

Acknowledgements We would like to express our heartfelt gratitude to Prof. Tian-Jue Zhang and Prof. Yin-Long Lü of the China Institute of Atomic Energy for their support in the experiment. We would also like to thank the accelerator team for providing high-quality proton beams.

References

1. F.A. Cucinotta, F.K. Manuel, J. Jones et al., Space radiation and cataracts in astronauts. Aviat. Space Environ. Med. **156**(5), 460–466 (2001). https://doi.org/10.1667/0033-7587(2001)156%5b0460:SRACIA%5d2.0.C0;2
2. F.A. Cucinotta, Space radiation risks for astronauts on multiple International Space Station missions. PLoS ONE **9**(4), e96099 (2014). https://doi.org/10.1371/journal.pone.0096099
3. R.S. Bobby, M.W. Dale, Y. Tesfaigzi et al., Mechanistic basis for nonlinear dose-response relationships for low-dose radiation-induced stochastic effects. Nonlinearity Biol. Toxicol. Med. **1**(1), 93–122 (2003). https://doi.org/10.1080/15401420390844492
4. K. Baverstock, A.V. Karotki, Towards a unifying theory of late stochastic effects of ionizing radiation. Mutat. Res. **718**(1–2), 1–9 (2010). https://doi.org/10.1016/j.mrgentox.2010.11.003
5. R.S. Bobby, M.W. Dale, V.E. Walker, Low-dose radiation and genotoxic chemicals can protect against stochastic biological effects. Nonlinearity Biol. Toxicol. Med. **2**(3), 185 (2004). https://doi.org/10.1080/15401420490507602
6. L.W. Townsend, R.J.M. Fry, Radiation protection guidance for activities in low-earth orbit. Adv. Space Res. **30**(4), 957–963 (2002). https://doi.org/10.1016/S0273-1177(02)00160-6
7. Y.N. Liu, H.S. Ye, W. Li et al., Review of measurement technique for dosimetry in space. J. Astronaut. Metrol. Meas. **33**(5), 68–73 (2013). https://doi.org/10.3969/j.issn.1000-7202.2013.05.015. **(in Chinese)**
8. E.R. Benton, E.V. Benton, A.L. Frank, Passive dosimetry aboard the Mir Orbital Station: external measurements. Radiat. Meas. **35**(5), 457–471 (2002). https://doi.org/10.1016/S1350-4487(02)00076-8
9. O. Goossens, F. Vanhavere, N. Leys et al., Radiation dosimetry for microbial experiments in the International Space Station using different etched track and luminescent detectors. Radiat. Prot. Dosim. **120**(1–4), 433–437 (2006). https://doi.org/10.1093/rpd/nci652
10. T. Doke, T. Hayashi, S. Nagaoka et al., Estimation of dose equivalent in STS-47 by a combination of TLDS and CR-39. Radiat. Meas. **24**(1), 75–82 (1995). https://doi.org/10.1016/1350-4487(94)00084-E
11. T. Hayashi, T. Doke, J. Kikuchi et al., Measurement of LET distribution and dose equivalent on board the Space Shuttle STS-65. Radiat. Meas. **26**(6), 935–945 (1996). https://doi.org/10.1016/S1350-4487(96)00095-9
12. H. Yasuda, Effective dose measured with a life size human phantom in a low Earth orbit mission. J. Radiat. Res. **50**(2), 89–96 (2009). https://doi.org/10.1269/jrr.08105
13. H. Yasuda, D.B. Gautam, T. Komiyama et al., Effective dose equivalent on the Ninth Shuttle-Mir mission (STS-91). Radiat. Res. **154**(6), 705–713 (2000). https://doi.org/10.1667/0033-7587(2000)154%5b0705:EDEOTN%5d2.0.CO;2
14. G.D. Badhwar, W. Atwell, F.F. Badavi et al., Space radiation absorbed dose distribution in a human phantom. Radiat. Res. **157**(1), 76–91 (2002). https://doi.org/10.1667/0033-7587(2002)157%5b0076:SRADDI%5d2.0.CO;2
15. G. Dietze, D.T. Bartlett, D.A. Cool et al., Assessment of radiation exposure of astronauts in Space, ICRP publication 123 (Oxford Britain, 2013). https://doi.org/10.1016/j.icrp.2013.05.004
16. G.P. Ginet, T.P. O'Brien, D.L. Byers, AP-9/AE-9: new radiation specification models, http://lws-set.gsfc.nasa.gov/documents. Accessed 2 Apr 2016
17. F.B. Francis, Validation of the new trapped environment AE9/AP9/SPM at low Earth orbit. Adv. Space Res. **54**(6), 917–928 (2014). https://doi.org/10.1016/j.asr.2014.05.010
18. N.P. Henss, W.E. Bolch, K.F. Eckerman et al., Conversion coefficients for radiological protection quantities for external radiation exposures, ICRP publication 116 (Oxford Britain, 2010). https://doi.org/10.1016/j.icrp.2011.10.001
19. H.G. Menzel, C. Clement, P. DeLuca, Realistic reference phantoms: an ICRP/ICRU joint effort, ICRP publication 110 (Oxford Britain, 2009). https://doi.org/10.1016/j.icrp.2009.09.001
20. J. Valentin, Basic anatomical and physiological data for use in radiological protection: reference values, ICRP publication 89 (Oxford Britain, 2002). https://doi.org/10.1016/s0146-6453(03)00002-2
21. C.Z. Wang, W.Y. Luo, Y.Z. Zha et al., Monte-Carlo simulation of optimization choice of shielding materials for proton radiation in space. Radiat. Prot. **27**(2), 79–86 (2007). https://doi.org/10.3321/j.issn:1000-8187.2007.02.003. **(in Chinese)**
22. G.H. Shen, S.J. Wang, S.Y. Zhang et al., A particles' direction detector on manned space II. Nucl. Electron. Detect. Technol. **32**(5), 535–538 (2012). https://doi.org/10.3969/j.issn.0258-0934.2012.05.009. **(in Chinese)**
23. Y. Kim, W. Atwell, A.J. Tylka et al., Radiation dose assessment of solar particle events with spectral representation at high energies for the improvement of radiation protection, in *38th COSPAR Scientific Assembly, Bremen, Germany* (2010)
24. B. Fraboni, A. Cavallini, W. Dusi, Damage induced by ionizing radiation on CdZnTe and CdTe detectors. IEEE Trans. Nucl. Sci. **51**(3), 1209–1215 (2004). https://doi.org/10.1109/TNS.2004.829445
25. J.R. Sabin, J. Oddershede, P. Sigmund, On the proton stopping power maximum in gases and vapours. Nucl. Instrum. Methods B **12**(1), 80–83 (1985). https://doi.org/10.1016/0168-583X(85)90704-9
26. L. Torrisi, Plastic scintillator investigations for relative dosimetry in proton-therapy. Nucl. Instrum. Methods B **170**(3), 523–530 (2000). https://doi.org/10.1016/S0168-583X(00)00237-8
27. C.S. Ji, *Handbook of nuclear radiation detectors and their experiment techniques* (Atomic Energy Press, Beijing, 1990), p. 315. **(in Chinese)**
28. National Institute of Standards and Technology, Stopping-power and range tables for protons, https://physics.nist.gov/PhysRefData/Star/Text/PSTAR.html. Accessed 18 Oct 2016
29. C.X. Kan, Y.M. Hu, Y.W. Bao et al., Annual Report of HI-13 Tandem Accelerator in 2013, Annual Report of China Institute of Atomic Energy 2013, Beijing, China, June, 2014. **(in Chinese)**
30. B.P. Denise, MCNPX^{TM} user's manual. LANL USA, LA-CP-07-1473, 2008